

State-selective electron capture in Kr^{8+} – $\text{Li}(2s)$ collisions for impact energies from 0.1 to 1.5 keV amu $^{-1}$

E Jacquet^{†‡}, M Chantepie^{†‡}, P Boduch^{†‡}, C Laulhé^{†‡}, D Lecler[†] and J Pascale[§]

[†] Centre Interdisciplinaire de Recherche Ions Lasers, UMR 6637 CEA, CNRS, ISMRA, Université de Caen, ISMRA, 6 boulevard Maréchal Juin, F-14050 Caen Cedex 4, France

[‡] UFR des Sciences, Université de Caen Basse Normandie, Esplanade de la Paix, F-14032 Caen Cedex, France

[§] Service des Photons, Atomes et Molécules, CEA, Centre d'Etudes de Saclay, Bâtiment 522, F-91191 Gif-sur-Yvette Cedex, France

Received 22 October 1998

Abstract. The 8ℓ - and 9ℓ -distributions of the Kr^{7+} -excited states resulting from single-electron capture in Kr^{8+} – $\text{Li}(2s)$ collisions are determined experimentally for collision energies from 0.1 to 1.0 keV amu $^{-1}$. The experimental $\sigma(n\ell)$ cross sections are deduced from emission cross sections obtained by means of near ultraviolet and visible photon spectroscopy. In addition, a complete theoretical study of these distributions has been made using the classical trajectory Monte Carlo (CTMC) method for a larger energy domain (0.1–5.0 keV amu $^{-1}$). The theoretical and experimental results are, on the whole, in fair agreement. The results are discussed in terms of dynamical couplings involved in state-selective electron capture from an analysis of electronic energy curves calculated for the $\{\text{Kr}^{7+} + \text{Li}\}^+$ system.

1. Introduction

Collisions of multiply charged ions with lithium atoms in the ground state or excited states are of fundamental interest for the understanding of the one-electron capture mechanisms. They can be of importance for obtaining information on magnetically confined fusion plasma properties (Brazuk *et al* 1985, Schweinzer *et al* 1992, Hoekstra 1995). Lithium beam spectroscopy can provide diagnostic information on the plasma edge properties and the plasma impurities. The detection of the resonance $2s$ – $2p$ transition in lithium ($\lambda = 670.8$ nm) allows the determination of electron densities (McCormick *et al* 1985, Aumayr *et al* 1992). Measuring the cross sections for state-selective electron capture from Li atoms injected in the plasma into highly excited states of plasma impurities allow the determination of the densities (Schorn *et al* 1991) and temperatures (Schorn *et al* 1992) of plasma impurities. These methods are connected to the knowledge of numerous data for collisions between multiply charged ions and lithium atoms in the low-energy range, in particular cross sections for single-electron capture (Wutte *et al* 1997). Visible photon spectroscopy is a convenient tool for studying single-electron capture from $\text{Li}(2s)$ atoms (Dijkkamp *et al* 1984, Wolfrum *et al* 1992, Hoekstra *et al* 1992, Rieger *et al* 1995). Together with these experimental studies, the classical trajectory Monte Carlo method (CTMC method) has been used to perform calculations for different systems (Olson *et al* 1992, Hoekstra *et al* 1993). For X^{6+} ($\text{X} \equiv \text{C}, \text{N}, \text{O}$ and Ne) projectiles, the total cross sections for the $n = 7 \rightarrow 6$ and $n = 8 \rightarrow 7$ transitions were measured and found to be

nearly independent of the core electrons of the projectile. Similar results were found in B^{5+} and N^{5+} -Li(2s) collisions.

For collisions with fully stripped ions (C^{6+} and O^{8+} , for example), states with large angular momenta are predominantly populated. Using an atomic-orbital close-coupling method, Schweinzer *et al* (1994) have calculated total single-electron capture cross sections for collisions between fully stripped ions and Li atoms. They have found a scaling formula which gives the total cross section with respect to the charge q of the incident ion and the initial binding energy of the electron in the Li target. This scaled total cross section is in agreement with theoretical and experimental data except for H^+ -Li(2s) collisions and is almost energy independent in the 1–10 keV amu^{-1} reduced energy range.

For Ar^{8+} -Li(2s) collisions, Jacquet *et al* (1995) have found that, in addition to states with large angular momenta, states with low ℓ values ($\ell \leq 3$) are populated. This result was attributed to a core-electron effect as predicted by CTMC calculations for N^{5+} and Ar^{8+} -Cs(6s) collisions (Pascale *et al* 1990) and observed experimentally (Martin *et al* 1992, Denis *et al* 1994). Moreover, in Ne^{8+} and Ar^{8+} -Na(3s) collisions, for the energy range 0.06–0.56 keV amu^{-1} for Ne^{8+} and 0.03–0.08 keV amu^{-1} for Ar^{8+} , the cross section for capture into the 9s level (and also the 9p level for Ar^{8+}) is higher than for capture into the higher ℓ levels (Gauntt and Danzmann 1992). In addition, the 9s and 9p cross sections for Ar^{8+} exhibit a maximum in the energy range 0.04–0.05 keV amu^{-1} , whereas the $\sigma(9s)$ cross section for Ne^{8+} shows an increase with decreasing energies.

In the last few years, we have studied state-selective electron capture process in collisions of Ar^{8+} ions on lithium atoms in the ground state. In particular, the effect of the projectile energy on the one-electron capture cross sections has been investigated (Jacquet *et al* 1995, Laulhé *et al* 1997), both experimentally, by means of visible photon spectroscopy, and theoretically, using CTMC calculations. In addition, with new data for confined plasma diagnostics, this collision system is a one-electron system consisting of a multicharged ion having a closed-shell core and an alkali-metal target having a loosely bound valence electron. The presence of Ar^{8+} core electrons removes the degeneracy of the corresponding hydrogenic states, all the $\sigma(n\ell)$ cross sections ($n = 8$ and 9) were deduced from emission line cross sections for collision energies between 0.1 and 4.5 keV amu^{-1} . The experimental results are, on the whole, in fair agreement with the CTMC calculations. This study has proved that the CTMC method, which is well adapted to the study of electron capture into excited levels, can also be used to predict state-selective cross sections in the low-energy range, where the *quasi-molecular* collision regime is reached. Both the experimental and the CTMC-calculated results have been analysed in terms of dynamical couplings using calculations of the electronic energies of the one-electron $\{Ar^{7+}-Li\}^+$ system. At low energies, the radial couplings at the avoided crossings between the entrance channel and the $\{Ar^{7+}(n\ell) + Li^+\}$ outgoing channels ($n = 8$ and 9 , $\ell = 0, 1, 2$) are efficient. As a result, the $\sigma(n\ell)$ cross sections increase with decreasing energies for a given $n\ell$ level and should go through a maximum. Indeed, for $\sigma(8s)$, this maximum is observed in both experimental and CTMC-calculated results and also for $\sigma(8p)$ in the CTMC results. Because of smaller energy splitting at the avoided crossings between the entrance molecular channel and the electron capture channels into 9s and 9p levels, no maximum has been observed in the $\sigma(9s)$ and $\sigma(9p)$ cross sections. As noticed above, these maxima were indeed observed at low energy in Ar^{8+} -Na(3s) collisions (in the 0.04–0.05 keV amu^{-1} energy range). The $\sigma(n\ell)$ cross sections for the largest values of ℓ decrease with decreasing energies.

For the Kr^{8+} -Li(2s) collisions studied here, the $\sigma(n\ell)$ cross sections should have an energy dependence similar to the case of Ar^{8+} -Li(2s) collisions. However, because of larger energy splitting at the avoided crossings between the entrance channel and the electron capture channels for Kr^{8+} than for Ar^{8+} , we expect maxima in the $\sigma(n\ell)$ cross sections for 8s and

8p at larger energies than for Ar^{8+} – $\text{Li}(2s)$ collisions. The maxima should also be visible for the $\sigma(9s)$ and $\sigma(9p)$ cross sections. However, in view of very different energy diagrams for Ar^{7+} and Kr^{7+} (see the discussion below), the relative magnitude of $\sigma(n\ell)$ cross sections for the Kr^{8+} – $\text{Li}(2s)$ collisions should be quite different from Ar^{8+} – $\text{Li}(2s)$ collisions. In addition to the study of the projectile energy effect, the effect of the projectile–core electrons on the one-electron cross sections will also be studied.

In this paper, we report experimental and CTMC-calculated results on the energy dependence of the Kr^{8+} – Li system for collision energies between 0.1 and 1.5 keV amu^{−1}. By comparison with the results already obtained for O^{8+} and Ar^{8+} – $\text{Li}(2s)$ collisions, the effects of the projectile–core electrons will be analysed. The experimental set-up and the method for the determination of experimental cross sections as well as the CTMC method to calculate the state-selective electron capture cross sections will be summarized. Calculations of the electronic energies of the one-electron $\{\text{Kr}^{7+}\text{Li}\}^+$ system performed using a pseudopotential method will be presented and the results for the state-selective electron capture cross sections will be discussed in terms of dynamical couplings. A preliminary molecular analysis of the state-selective electron capture cross sections in low-energy collisions of X^{8+} ions ($\text{X} \equiv \text{O}, \text{Ar}, \text{Kr}$) with $\text{Li}(2s)$ atoms has already been reported (Pascale *et al* 1997).

2. Experimental set-up

A detailed description of the entire experimental set-up can be found elsewhere (Jacquet *et al* 1994, Laulhé *et al* 1997), only the main points will be noted here. All the experiments were performed at the GANIL[†] test bench, the projectile ions were produced by an electron cyclotron resonance ion source (ECRIS), either a NANOGAN2 or an ECR4 ion source. After a charge and mass analysis, the Kr^{8+} ion beam was transported to the collision chamber by a magnetic triplet. The background pressure in the beam line and in the collision chamber was about 0.5×10^{-7} mbar. The effusive jet of lithium atoms was produced by heating up solid lithium to about 600 °C with a thermocoaxial cable. After crossing the target, the Kr^{8+} ion beam was collected by a Faraday cup in order to measure the ion beam current (between 50 and 100 μA). The observation direction was 90° with respect to the directions of the lithium jet and the ion beam. The emitted photons were focused on the entrance slit of a direct incidence grating spectrometer (SOPRA 700) equipped with a 1200 grooves/mm grating blazed for 750 nm in the first order. The photons were then detected by a photomultiplier (Hamamatsu R106) in the 200–600 nm wavelength range. The ECRIS used here could provide a Kr^{8+} ion beam for extracted potential between 7.5 and 16 kV, i.e. for energies between about 0.8 and 1.5 keV amu^{−1}. In order to record spectra for energies below 0.8 keV amu^{−1}, the Kr^{8+} ions were extracted from the ion source at the potential V_{ECR} and decelerated in the collision chamber. The potential V_{ECR} was chosen so that a strong and stable ion current was produced by the ion source. The decelerating device was composed of two asymmetric einzel lenses situated on both sides of the Li jet. Both of them were at the potential V_{lens} , the ion beam energy was then of $(V_{\text{ECR}} - V_{\text{lens}}) q$ eV in the collision area (just above the Li oven) and $V_{\text{ECR}} q$ eV after the decelerating device. Each asymmetric einzel lens was composed of three cylindrical electrodes, the first one was connected to the ground of the ion source, the second one to an intermediate potential V and the third one to the potential V_{lens} . As the ion beam was likely to explode under a strong charge-space effect, the intermediate lens was used to focus the ion beam on the collision area. With the ion beam line being at the ground of the ion source, it was necessary to place a second einzel lens after the collision area in order to accelerate the

[†] Grand Accélérateur national d'Ions lourds, Caen, France.

ion beam and measure its current with a Faraday cup. The potential was rather homogeneous in the collision area (for example, $V_{\text{lens}} - V_{\text{ECR}} = 250 \pm 3$ q eV) and 95% of the ion beam produced by the ion source was collected in the Faraday cup for the lower energy we had used in these experiments.

Spectra for collision energies between 0.1 and 1.5 keV amu⁻¹ were recorded. The spectral analyses of such emissions were presented in detail a few years ago (Jacquet *et al* 1994) and recently revised for lines between 560 and 590 nm corresponding to 8p–8d, 8d–8f, 7f–8d and 9p–8d transitions (Jacquet *et al* 1998). The emission cross section of each transition was determined using the spectroscopic response of the optical device and the absolute calibration of the line intensities. The response of our detection system takes into account the theoretical grating efficiency and the phototube response function given by the manufacturer. The absolute calibration of the line intensities was obtained previously (Jacquet *et al* 1993) by recording the spectra for 60 keV C⁴⁺–Li(2s) collisions and using the excitation cross sections for C³⁺($n\ell$) determined by Dijkkamp *et al* (1984). The relative uncertainties due to the calibration method and the polarization effects are always lower than $\pm 30\%$. As the Kr⁸⁺ ion beam and the lithium jet are stable, the uncertainties due to the calibration method are mainly due to the cross sections given by Dijkkamp *et al* (1984). The polarization effects are difficult to evaluate: they depend on the wavelength of the transition, on the diffraction order of the spectrometer grating and on the polarization of the detected lines. If we assume that the polarization rates of the C³⁺ and the Kr⁷⁺ lines are of the same order, the polarization uncertainties are probably small and an upper limit of 30% for the relative uncertainties seems large enough to us to take the errors into account.

3. Single-electron capture cross sections

3.1. Experimental results

The experimental emission cross sections of the single-electron capture lines are given in table 1 for projectile energies between 0.1 and 1.5 keV amu⁻¹. The $\sigma(n\ell)$ cross sections for single-electron capture into the most populated $n = 8$ and 9 states are reported in table 2. They were deduced from emission cross sections and transition probabilities. The transition probabilities were calculated from radial matrix elements obtained with the parametric potential method of Klapish (1971) optimized with some energy levels from Reader *et al* (1991). The potential used in the evaluation of radial matrix elements can be found in Jacquet *et al* (1994). For each $\sigma(n\ell)$ cross section, the uncertainty was deduced from the uncertainties of the emission cross sections. For example,

$$\begin{aligned}\sigma(8f) &= \frac{\sigma_{\text{em}}(8d-8f)}{b_{8d-8f}} - \sigma_{\text{em}}(8f-9g) - \sigma_{\text{em}}(8f-9d) \\ \sigma(8f) &= \frac{\sigma_{\text{em}}(8d-8f)}{b_{8d-8f}} - \sigma_{\text{em}}(8f-9g) - \frac{b_{8f-9d}}{b_{8p-9d}} \sigma_{\text{em}}(8p-9d)\end{aligned}$$

where b_{i-j} is the branching ratio of the j state to the i state,

$$\Delta\sigma(8f) = \frac{\Delta\sigma_{\text{em}}(8d-8f)}{0.338} + \Delta\sigma_{\text{em}}(8f-9g) + \frac{0.137}{0.023} \Delta\sigma_{\text{em}}(8p-9d).$$

3.2. CTMC-calculated cross sections

Cross sections for capture into the different $n\ell$ sublevels were calculated using the CTMC method (Abrines and Percival 1966, Olson and Salop 1977). The three particles involved in

Table 1. Experimental emission cross sections (10^{-16} cm^2) versus the projectile energy (keV amu^{-1}) for single-electron capture following Kr^{8+} -Li(2s) collisions. The experimental uncertainties are always lower than 30%.

Transition	Energy					
	0.1	0.2	0.5	0.8	1.0	1.5
6s-6p	0.50	0.69	0.64	0.49	0.38	0.64
6p-6d	13.44	16.34	15.44	13.07	11.02	20.06
6d-6f	18.88	18.47	22.32	15.98	11.52	21.85
7p-7d	5.87	7.44	8.30	6.92	6.03	10.43
7d-7f	7.90	10.16	11.53	12.26	9.74	14.74
8p-8d	13.57	10.70	11.56	12.45	14.81	18.05
8d-8f	34.70	22.90	10.48	9.03	10.64	11.39
5f-6d	7.36	8.04	9.15	7.64	6.21	9.62
6d-7p	2.44	3.09	3.89	3.00	1.99	4.41
6f-7d	3.72	4.53	4.94	4.61	3.74	6.48
7p-8s	0.14	0.21	0.31	0.49	0.70	1.39
7d-8p	2.39	3.64	5.64	4.43	3.91	5.64
7f-8d	8.86	8.44	8.26	8.99	10.20	11.63
7f-8g	1.28	1.29	0.59	0.67	0.46	0.88
7g-8f	2.55	3.12	1.47	1.07	0.94	1.45
7g-8h	3.99	5.56	5.26	4.72	4.90	10.50
7h-8i	8.03	15.05	20.36	25.29	20.99	36.62
7i-8k	15.39	38.96	69.66	71.55	51.68	66.76
8p-9s	1.39	3.98	5.81	3.10	1.98	2.61
8p-9d	1.74	1.49	1.32	1.41	1.03	1.16
8d-9p	5.61	3.94	3.36	3.40	2.91	3.43
8d-9f	1.36	1.74	0.97	0.57	0.49	0.70
8f-9g	0.35	0.52	0.39	0.28	0.26	0.46
8g-9h	0.77	1.53	1.64	1.40	1.57	2.92
8h-9i	1.54	4.00	6.70	6.14	5.88	12.81
8i-9k	1.78	4.59	13.25	9.64	6.97	20.83
8k-9l	2.46	9.84	19.27	22.04	13.20	31.28

the collision (the valence electron and the two ionic cores Li^+ and Ar^{8+}) are treated classically. The Hamiltonian equations are solved for initial conditions which are chosen pseudo-randomly (Monte Carlo method) for the projectile and the target (Pascale *et al* 1990, Olson *et al* 1992). Each set of initial conditions defines the so-called classical trajectory. Model potentials have been used to describe the interactions between the valence electron and the two ionic cores and the method of Reinhold and Falcon (1986) has been used to define the initial conditions of the target. For the e^-Li^+ interaction, the model potential determined by Klapish (1971) was used; for the e^-Kr^{8+} interaction, we have used the model potential determined previously (Jacquet *et al* 1994)

$$V_{Kr^{8+}} = -\frac{1}{r} (8 + 28e^{-4.75r} + 5.7re^{-3.52r})$$

where the parameters have been determined to fit Kr^{7+} energy levels to a good approximation.

The binding procedure used to determine the final quantum numbers n and ℓ from the classical angular momentum and the classical binding energy of the relative electron to the projectile-core Kr^{8+} has already been described (Jacquet *et al* 1995). It takes into account asymptotic quantum defects of the $n\ell$ Kr^{7+} energy levels (Theodosiou *et al* 1986):

Table 2. Experimental cross sections (10^{-16} cm^2) versus the projectile energy (keV amu^{-1}) for single-electron capture into the 8ℓ and 9ℓ sublevels for Kr^{8+} -Li(2s) collisions.

$n\ell$	Energy					
	0.1	0.2	0.5	0.8	1.0	1.5
8s	0.1 ± 0.5	0.6 ± 0.7	1.1 ± 0.9	2.5 ± 1.2	4.0 ± 1.6	8.6 ± 3.1
8p	2.0 ± 11.5	13.8 ± 14.2	27.5 ± 20.2	18.6 ± 16.8	14.4 ± 15.4	25.6 ± 20.8
8d	11.7 ± 27.3	21.4 ± 22.9	33.5 ± 18.9	34.1 ± 17.7	45.7 ± 21.9	57.2 ± 26.5
8f	81.5 ± 30.6	52.1 ± 21.1	19.3 ± 10.6	15.4 ± 9.6	21.7 ± 10.2	26.3 ± 12.2
8g	9.9 ± 3.9	9.1 ± 4.2	3.2 ± 2.3	4.3 ± 2.3	2.3 ± 1.8	4.6 ± 3.4
8h	11.8 ± 4.5	14.6 ± 6.8	10.9 ± 7.3	9.7 ± 6.6	10.6 ± 6.7	22.4 ± 14.4
8i	12.5 ± 4.8	22.1 ± 9.4	22.9 ± 14.8	35.3 ± 16.4	30.3 ± 13.3	44.2 ± 25.8
8k	12.9 ± 3.9	29.1 ± 8.7	50.4 ± 15.1	49.5 ± 14.9	38.5 ± 11.6	35.4 ± 10.7
Total $n = 8$	142.4 ± 87.0	162.9 ± 88.0	168.7 ± 90.1	169.3 ± 85.5	167.4 ± 82.5	224.3 ± 116.7
9s	13.2 ± 5.5	37.9 ± 12.4	55.4 ± 16.6	29.6 ± 8.9	18.9 ± 5.7	24.9 ± 7.5
9p	74.6 ± 23.9	52.3 ± 16.7	51.1 ± 15.3	43.7 ± 13.1	42.7 ± 12.8	39.0 ± 11.7
9d	75.6 ± 22.7	64.8 ± 19.5	57.4 ± 17.2	61.5 ± 18.4	44.7 ± 13.4	50.7 ± 15.2
9f	12.7 ± 3.8	16.3 ± 4.9	9.0 ± 2.7	5.3 ± 1.6	4.5 ± 1.4	6.5 ± 2.0
9g	5.1 ± 1.5	7.6 ± 2.3	5.8 ± 1.7	4.1 ± 1.2	3.9 ± 1.2	6.7 ± 2.0
9h	4.0 ± 1.2	8.0 ± 2.4	8.6 ± 2.6	7.3 ± 2.2	8.2 ± 2.5	15.3 ± 4.6
9i	4.5 ± 1.3	11.7 ± 3.5	19.5 ± 5.9	17.9 ± 5.4	17.1 ± 5.1	37.3 ± 11.2
9k	2.9 ± 0.9	7.6 ± 2.3	21.9 ± 6.6	15.9 ± 4.8	11.5 ± 3.5	34.4 ± 10.3
9l	2.3 ± 0.8	9.6 ± 3.0	18.6 ± 6.0	20.7 ± 7.0	12.1 ± 4.3	28.3 ± 10.3
Total $n = 9$	195.1 ± 61.6	215.8 ± 67.0	247.2 ± 74.5	206.0 ± 62.6	163.6 ± 49.8	243.1 ± 74.7

Table 3. CTMC-calculated cross sections (10^{-16} cm^2) versus the projectile energy (keV amu^{-1}) for single-electron capture into the 8ℓ and 9ℓ sublevels for Kr^{8+} -Li(2s) collisions.

$n\ell$	Energy									
	0.1	0.2	0.5	0.8	1.0	1.43	2.0	3.0	4.0	5.0
8s	0.77	1.23	2.23	2.64	3.35	3.31	3.79	4.43	4.03	2.90
8p	6.36	7.72	13.14	15.29	15.30	15.48	14.80	11.83	10.82	8.41
8d	31.81	39.50	49.39	51.23	50.33	45.56	41.67	32.54	24.99	19.57
8f	84.87	70.14	51.59	41.10	38.72	33.62	27.27	21.86	16.08	12.95
8g	36.27	22.77	11.42	9.82	9.29	9.35	8.05	6.11	5.77	5.30
8h	18.47	16.80	14.42	16.23	16.82	18.00	17.20	14.34	14.01	16.77
8i	25.11	24.26	27.48	30.47	30.57	27.31	25.19	27.37	32.92	38.16
8k	24.88	42.43	43.38	38.11	38.65	37.82	43.78	46.71	46.09	44.35
Total $n = 8$	228.5	224.8	213.1	204.9	203.0	190.5	181.7	165.2	154.7	148.4
9s	17.34	17.67	20.34	19.53	18.06	16.61	14.38	10.96	7.28	5.03
9p	82.25	78.17	72.23	62.88	56.07	44.74	31.97	20.44	13.32	8.87
9d	114.97	106.8	89.63	77.08	69.57	57.40	46.51	30.62	12.29	13.30
9f	49.19	40.04	29.82	26.33	24.62	22.29	17.95	13.02	9.40	7.69
9g	11.47	9.95	7.35	6.53	6.85	6.22	5.39	5.94	5.68	5.04
9h	6.77	8.31	9.04	11.28	12.00	14.22	14.37	15.31	14.44	12.91
9i	9.42	10.89	14.53	20.57	22.40	26.08	25.42	27.60	33.72	39.71
9k	9.64	11.47	17.89	25.90	28.01	33.25	37.88	48.46	61.42	66.92
9l	4.80	8.58	12.65	16.11	18.82	28.18	49.57	59.13	61.68	55.64
Total $n = 9$	305.9	291.9	273.5	266.2	256.4	249.0	243.5	231.5	226.2	215.1

$\delta(0) = 1.3205$, $\delta(1) = 1.1041$, $\delta(2) = 0.6699$, $\delta(3) = 0.1159$ and $\delta(\ell \geq 4) = 0$. The number of trajectories (between 7.5×10^4 and 1.25×10^5 trajectories, depending on the projectile

Table 4. CTMC-calculated emission cross sections (10^{-16} cm^2) versus the projectile energy (keV amu^{-1}) for single-electron capture following $\text{Kr}^{8+}\text{-Li}(2s)$ collisions.

Transition	Energy					
	0.1	0.2	0.5	0.8	1.0	1.43
6s–6p	0.343	0.318	0.281	0.249	0.239	0.209
6p–6d	11.988	11.286	10.529	9.679	9.303	8.354
6d–6f	21.414	18.893	16.532	15.609	15.167	14.283
7p–7d	8.829	8.064	7.635	7.227	7.083	6.735
7d–7f	13.409	13.746	14.669	14.339	14.622	13.372
8p–8d	10.233	11.613	13.359	13.449	13.077	11.742
8d–8f	34.405	28.945	21.857	17.696	16.565	14.284
5f–6d	5.007	4.713	4.397	4.042	3.885	3.489
6d–7p	1.565	1.522	1.456	1.413	1.372	1.323
6f–7d	5.192	4.742	4.490	4.249	4.165	3.960
7p–8s	0.480	0.508	0.550	0.550	0.640	0.600
7d–8p	1.775	1.858	2.372	2.526	2.476	2.401
7f–8d	7.365	8.358	9.614	9.679	9.411	8.451
7f–8g	4.571	3.040	1.719	1.581	1.542	1.596
7g–8f	6.603	5.555	4.194	3.396	3.179	2.741
7g–8h	6.574	6.260	5.991	7.280	7.722	8.635
7h–8i	17.718	17.988	22.166	26.974	27.925	28.479
7i–8k	30.575	51.540	57.046	56.360	59.856	70.640
8p–9s	1.963	1.976	2.197	2.087	1.937	1.769
8p–9d	2.654	2.445	2.062	1.773	1.602	1.323
8d–9p	7.526	7.131	6.533	5.677	5.071	4.040
8d–9f	5.284	4.302	3.213	2.838	2.658	2.415
8f–9g	0.807	0.704	0.526	0.474	0.504	0.465
8g–9h	1.317	1.620	1.791	2.266	2.426	2.910
8h–9i	3.382	3.965	5.269	7.521	8.234	9.690
8i–9k	6.106	7.208	11.305	16.520	17.888	21.733
8k–9l	5.413	8.900	13.196	17.460	20.366	31.301

energy) used in the calculations is taken as sufficiently large to ensure small statistical errors. These errors are smaller than about 5% for the most populated $n\ell$ levels ($n = 7, 8, 9$ and 10); for the lowest cross sections ($\sigma(8s)$ for example), they are between 6% and 13% for all the energies investigated.

The CTMC-calculated final $n\ell$ -distributions for $n = 8$ and 9 are reported in table 3 for the $\text{Kr}^{8+}\text{-Li}(2s)$ collisions at all the projectile energy values investigated experimentally. In order to show clearly the effect of the projectile energy on the cross sections, CTMC results obtained for energies in the $2.0\text{--}5.0 \text{ keV amu}^{-1}$ energy range are also reported in the table. The resulting CTMC-calculated emission cross sections of the experimentally observed lines are given in table 4 for comparison with the measured emission cross sections (table 1).

Before discussing the CTMC final $n\ell$ -distributions, let us consider first the CTMC cross sections $\sigma(n)$ for electron capture into a specific n level and the total capture cross section $\sigma_{\text{tot}} = \sum_n \sigma(n)$. They are reported in table 5 for the $0.1\text{--}5.0 \text{ keV amu}^{-1}$ energy range.

As for $\text{Ar}^{8+}\text{-Li}$ collisions (Laulhé *et al* 1997), the total cross section σ_{tot} decreases with increasing energies. The reduced cross section $\bar{\sigma}_{\text{tot}} = (4I_t^2/q)\sigma_{\text{tot}}$ (Schweitzer *et al* 1994) where q is the charge of the projectile and I_t the ionization potential of the target (in au) has been calculated; it varies (see table 5) from $1.23 \times 10^{-15} \text{ cm}^2$ for the lowest energy (0.1 keV amu^{-1})

Table 5. CTMC-calculated cross sections (10^{-16} cm^2) for single-electron capture into n levels in Kr^{8+} –Li(2s) collisions, versus the projectile energy (keV amu^{-1}). The total single-electron capture cross section and the reduced cross section (cm^2) are also reported (see Schweinzer *et al* 1994).

n	Energy									
	0.1	0.2	0.5	0.8	1.0	1.43	2.0	3.0	4.0	5.0
6	0.14	0.35	1.08	2.02	2.45	3.32	4.50	5.36	5.68	6.06
7	14.61	19.59	29.71	33.72	35.82	37.27	38.75	39.75	38.91	39.21
8	228.54	224.84	213.05	204.9	203.03	190.46	181.75	165.22	154.71	148.43
9	305.86	291.92	273.49	266.2	256.40	249.02	243.46	231.48	226.24	215.10
10	72.83	64.76	47.46	40.22	40.17	40.03	39.15	46.64	50.43	57.14
11	3.81	4.64	4.46	4.65	5.98	7.33	7.59	10.90	11.00	12.07
12	0.87	1.07	0.97	1.29	1.78	2.13	2.50	4.51	4.34	4.74
Total ($\times 10^{-14}$)	6.28	6.09	5.72	5.55	5.47	5.34	5.22	5.10	4.99	4.91
$\sigma_{\text{reduced}} (\times 10^{-15})$	1.23	1.20	1.12	1.09	1.07	1.05	1.02	1.00	0.98	0.96

to $0.96 \times 10^{-15} \text{ cm}^2$ at 5.0 keV amu^{-1} . In the $1\text{--}4 \text{ keV amu}^{-1}$ energy range, the reduced cross section is the same as the cross sections obtained for Ar^{8+} and O^{8+} –Li collisions (almost $1.0 \times 10^{-15} \text{ cm}^2$). These results are in agreement with the scaling formula of Schweinzer *et al* (1994) which predicts a reduced total cross section of $9.0 \times 10^{-16} \text{ cm}^2$ for all the present energy range.

As already observed for O^{8+} and Ar^{8+} –Li(2s) collisions (Laulhé *et al* 1997), the n distributions are mainly peaked on $n = 8$ and 9 , and as the projectile energy increases, they broaden towards higher and lower n values. Figures 1(a) and (b) show the experimental results for $\sigma(n)$ for $n = 8$ and 9 together with the CTMC results for O^{8+} and Ar^{8+} projectiles (Laulhé *et al* 1997) and Kr^{8+} projectiles. For Kr^{8+} –Li(2s) collisions, experimental and CTMC-calculated cross sections are in fair agreement for electron capture into $n = 8$, except for the lowest energy (0.1 keV amu^{-1}). For electron capture into $n = 9$, the CTMC results are well outside the experimental error bars for 0.1 and 1.0 keV amu^{-1} . For the three projectiles (O^{8+} , Ar^{8+} and Kr^{8+}), the CTMC-calculated $\sigma(8)$ cross section decreases continuously with increasing energies as does the $\sigma(9)$ cross section for Kr^{8+} , while the CTMC-calculated $\sigma(9)$ cross sections for O^{8+} and Ar^{8+} go through a maximum at about 1.0 keV amu^{-1} . Above 2.0 keV amu^{-1} , the $\sigma(8)$ and $\sigma(9)$ cross sections go, respectively, to the same value for the three projectiles. However, for the lowest energies, the $\sigma(8)$ cross sections are larger for Ar^{8+} than for O^{8+} and Kr^{8+} , while the $\sigma(9)$ cross sections are larger for Kr^{8+} than for O^{8+} and Ar^{8+} . Figure 1(c) shows the CTMC results for single-electron capture into the $n = 10$ level for O^{8+} , Ar^{8+} and Kr^{8+} –Li(2s) collisions. The energy dependence of the $\sigma(10)$ cross section for the Kr^{8+} projectile is seen to be very different from those for the O^{8+} and Ar^{8+} projectiles. Indeed, for Kr^{8+} –Li collisions, the $\sigma(10)$ cross section decreases for energies varying from 0.1 to 2.0 keV amu^{-1} and then increases in the $2.0\text{--}5.0 \text{ keV amu}^{-1}$ energy range, whereas the $\sigma(10)$ cross sections decrease continuously in the energy range for the O^{8+} and Ar^{8+} projectiles. For the highest energies, the $\sigma(10)$ cross sections go to the same value for the three projectiles.

The difference in the energy dependence of the 10 distribution will be explained later on by the competition between the effect of the projectile-core electrons and the Stark effect. For the highest energies investigated here, the projectile-core-electron effect vanishes and the Stark effect (which does not depend on the ionic projectile involved in the collision) dominates. As a result, the $\sigma(n)$ cross sections go to the same value for the three projectiles at high energies. This remark is also valid for the eight- and nine-distributions.

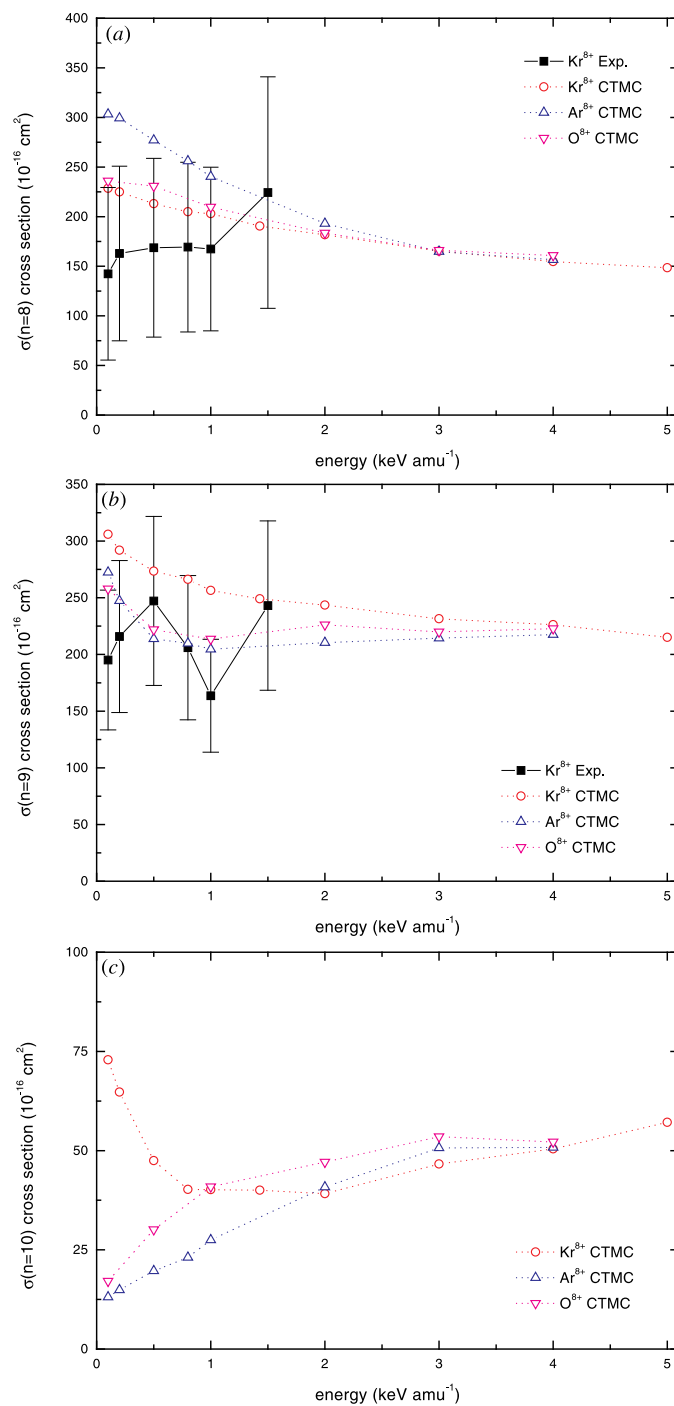


Figure 1. Experimental and CTMC-calculated $\sigma(n)$ cross sections (10^{-16} cm^2) for O^{8+} , Ar^{8+} and Kr^{8+} -Li(2s) collisions versus the projectile energy (keV amu^{-1}). The curves have been drawn to help guide the eye. (a) $n = 8$; (b) $n = 9$; (c) $n = 10$.

4. $n\ell$ distributions and the charge exchange process

In order to analyse more precisely the relative importance of the radial and rotational couplings on Stark mixing and the projectile-core-electron effect involved in both the primary capture process and in the outgoing channels, we present calculations of the electronic energies of the one-electron $\{\text{Kr}^{7+} + \text{Li}\}^+$ system. The adiabatic electronic energies of the one-electron $\{\text{X}^{7+} + \text{Li}\}^+$ ($\text{X} \equiv \text{O}, \text{Ar}$) have already been presented (Laulhé *et al* 1997). They have been determined from a linear combination of atomic orbitals (LCAO) calculations using a pseudopotential method (see Laulhé *et al* (1997), where the pseudopotential for the e^- -Li interaction can be found). For the e^- - Kr^{8+} interaction, we have used

$$V = \sum_{\ell} V_{\ell}(r) \mathcal{P}_{\ell} - \frac{8}{r} - \frac{\alpha_d r^2}{2(r^3 + r_c^3)^2}$$

where $\alpha_d = 0.2021$ au is the static dipole polarizability of the core Kr^{8+} (Johnson *et al* 1983) and the cut-off radius $r_c = 0.454$ au is approximately equal to the core radius (Desclaux 1973).

\mathcal{P}_{ℓ} is an angular momentum projector on the Kr^{8+} core and $V_{\ell}(r)$ is a Gaussian-type pseudopotential: $V_{\ell}(r) = A_{\ell} \exp(-B_{\ell} r^2)$. $A_{\ell} = 74.371, 47.022, 14.318$ and -8.586 for $\ell = 0, 1, 2$ and $\ell \geq 3$, respectively, $B_{\ell} = 4.439, 3.673, 2.303$ and 3.097 for $\ell = 0, 1, 2$ and $\ell \geq 3$, respectively. In the atomic basis-state expansion of the total electronic wavefunction for the $\{\text{Kr}^{7+} + \text{Li}\}^+$ system, all the wavefunctions for the Kr^{7+} ion from the ground state up to the $n = 12$ level have been considered. For the Li atom, the 2s, 3s, 2p, 3p and 3d wavefunctions have been considered.

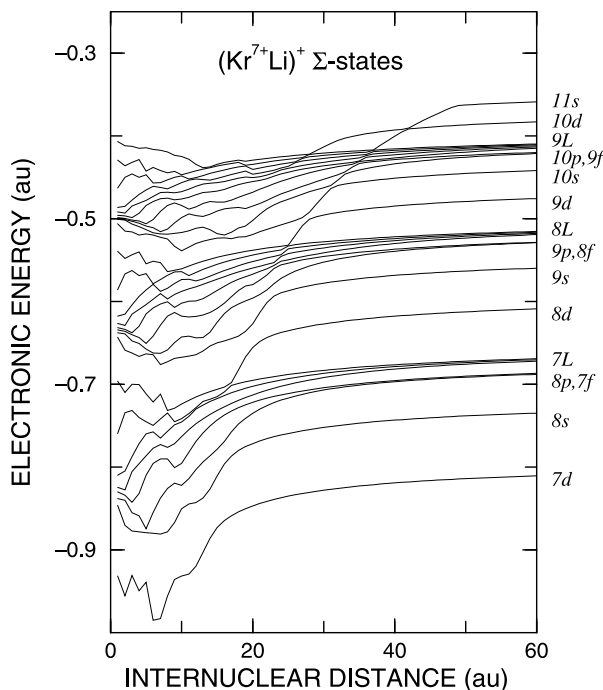


Figure 2. Calculated electronic energies (au) versus the internuclear distance (au) for $\{\text{Kr}^{7+} + \text{Li}\}^+$ Σ -states.

The core–core interaction, mainly the $8/R$ repulsive interaction, has not been considered in the calculations since it does not contribute to the non-adiabatic couplings between the molecular states. For the internuclear distance range $R = 0.1\text{--}60$ au, the molecular energy curves of the $\{\text{Kr}^{7+} + \text{Li}\}^+$ system were calculated for the Σ symmetry of the system. The Σ -state electronic energies relevant to the capture into the $n = 7, 8$ and 9 states of Kr^{7+} are plotted versus the internuclear distance (figure 2). In the separated atom limit, e.g. at very large internuclear distances, the entrance channel is the valence state $2s$ of the lithium atom and the various exit channels are correlated with the various levels of the Kr^{7+} ion. Moreover, the curve correlated with the $11s$ level of Kr^{7+} , which, in the separated atom limit, goes to the $2s$ level of Li through numerous diabatic crossings, is the entrance channel for the electron capture process. The degeneracy of the levels for $\ell \leq 3$ is removed by the core electrons in the separated atom limit. This effect has already been observed for the $\{\text{Ar}^{7+} + \text{Li}\}^+$ system, but is much stronger here since Kr^{8+} ions have 28 electrons (only 10 electrons for Ar^{8+} ions). The main difference from the $\{\text{Ar}^{7+} + \text{Li}\}^+$ system comes from the overlapping of various manifolds of molecular energy curves. The energy diagram of Kr^{7+} shows some particular features: the $8s$ and the $8p$ level energies are lower than the 7ℓ level energies ($\ell \geq 4$), and the $8p$ level is even quasi-degenerate with the $7f$ level ($\Delta E \approx 253 \text{ cm}^{-1}$). Moreover, the $8d$ level is above the 7ℓ ($\ell \geq 4$) levels. Similar observations on the relative positions of the levels can be made for any manifold of levels, in particular for $n = 9$. The $9p$ level is also quasi-degenerate with the $8f$ level ($\Delta E \approx 33 \text{ cm}^{-1}$). Finally, we noticed that the curve correlating with the $10s$ level is situated just below the $10p$ and $9f$ levels which are quasi-degenerate and the 9ℓ -manifold ($\ell \geq 3$), while the $7d$ level is just below the $8s$ level.

The Σ -electronic energy curves show up several avoided crossings with the entrance channel and among themselves in the region of $15\text{--}20$ au for those correlating with $7d$, $8s$, $8p$, $7f$ and $8d$ levels and in the region $22\text{--}32$ au for those correlating with $9s$, $9d$, $8f$, $9d$ and

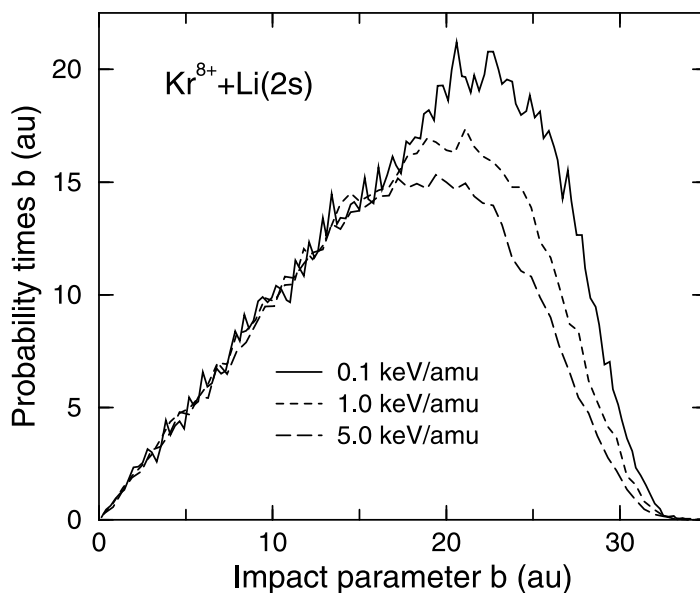


Figure 3. CTMC-calculated total electron capture probability times the impact parameter b versus b for $\text{Kr}^{8+}\text{-Li}(2s)$ collisions for projectile energies $E = 0.1, 1.0$ and 5.0 keV amu^{-1} .

10s levels. These avoided crossings are responsible for the primary radial couplings leading to electron capture into the $n = 8$ and 9 levels, but also into the 10s, 7d and 7f levels. The internuclear range of radial couplings agrees with the maximum impact parameter b , which contributes to the total electron capture cross section (see figure 3). At the lowest energies, the impact parameter corresponding to the maximum in the total electron capture probability times b is shifted at large b and the value of the maximum is also enhanced. This means that more upper electron capture channels contribute to the total electron capture cross sections when the energy decreases (for example, the 10s, 10p, 9d and 9f levels) because the radial couplings involving these electron capture channels become more efficient. The CTMC-calculated cross sections for electron capture into these levels decrease quickly with increasing energies in the energy range considered here. The projectile-core-electron effect is then responsible for the population of states of low ℓ values. This explains the differences in the energy dependence of the $\sigma(n)$ cross sections observed above (section 3) for the three projectiles O^{8+} , Ar^{8+} and Kr^{8+} . For O^{8+} - and Ar^{8+} -Li(2s) collisions, an analysis of the electronic energy curves (Laulhé *et al* 1997) indicates that the population of the $n = 10$ level results mainly from the Stark effect, so that the $\sigma(10)$ cross sections increase with increasing energies for both collisional systems over all of the energy range (figure 1(c)). For Kr^{8+} -Li(2s) collisions, the $\sigma(10)$ cross section increases with increasing energies in the high-energy range where the Stark effect dominates, and increases with decreasing energies in the low-energy range due to the projectile-core-electron effect populating the 10s and 10p levels (figure 4(b)); it then results in a minimum in the cross section at intermediate energies (figure 1(c)). This energy dependence of the $\sigma(10)$ cross section for Kr^{8+} projectiles is similar to that observed in the $\sigma(9)$ cross section for O^{8+} and Ar^{8+} projectiles (figure 1(b)). For Kr^{8+} projectiles, the $\sigma(9)$ cross section increases continuously with decreasing energies because of a larger contribution of the core-electron effect for populating the lowest ℓ -values over a larger energy range (see table 3) than for O^{8+} and Ar^{8+} projectiles (Jacquet *et al* 1995, Laulhé *et al* 1997), due to larger energy splittings for Kr^{8+} projectiles at the avoided crossings between the entrance channel and the electron capture channels for $n = 9$. For the same reasons as given above, the contribution of the core-electron effect over the whole energy range (which is stronger for Kr^{8+} than for Ar^{8+} and O^{8+} projectiles) causes the $\sigma(8)$ cross section for Kr^{8+} projectiles to increase more quickly with decreasing energies than for Ar^{8+} and O^{8+} projectiles, and, likewise, the $\sigma(9)$ cross section for Kr^{8+} projectiles.

The electron capture cross sections into the 7d, 7f and 10s levels for Kr^{8+} -Li(2s) collisions, which have been determined from the CTMC calculations (see figures 4(a) and (b)), could not be deduced from experimental emission cross sections. Within the $n = 7$ level (see figure 4(a)), the 7f sublevel is the most populated sublevel at almost all energies, and the population of 7d sublevels increases with energy because of the large energy splittings at the relevant avoided crossings. For the $n = 8$ levels (see figure 5 and table 3), the 8f level is also the most populated sublevel at the lowest energy. For the $n = 10$ level (see figure 4(b)), only the $\ell = 0$ and 1 sublevels are preferentially populated by rotational couplings. Due to the quasi-degeneracy of the 8p and 7f states on the one hand, and of the 9p and 8f states on the other hand, the experimental cross sections into the 8ℓ and 9ℓ states is rather difficult and may explain some discrepancies observed between the experimental and CTMC results (see figures 5 and 6, and tables 2 and 3).

Analysis of the CTMC-calculated $\sigma(n\ell)$ cross sections for Kr^{8+} -Li(2s) collisions versus the projectile energy is quite interesting. Indeed, as expected in the introduction, the $\sigma(n\ell)$ cross sections for electron capture into the lowest non-degenerate $n\ell$ levels go through a maximum with increasing energy. Thus, the $\sigma(7d)$ cross section goes through a broad maximum at $E \approx 4 \text{ keV amu}^{-1}$, as does the $\sigma(8s)$ cross section at $E \approx 3 \text{ keV amu}^{-1}$,

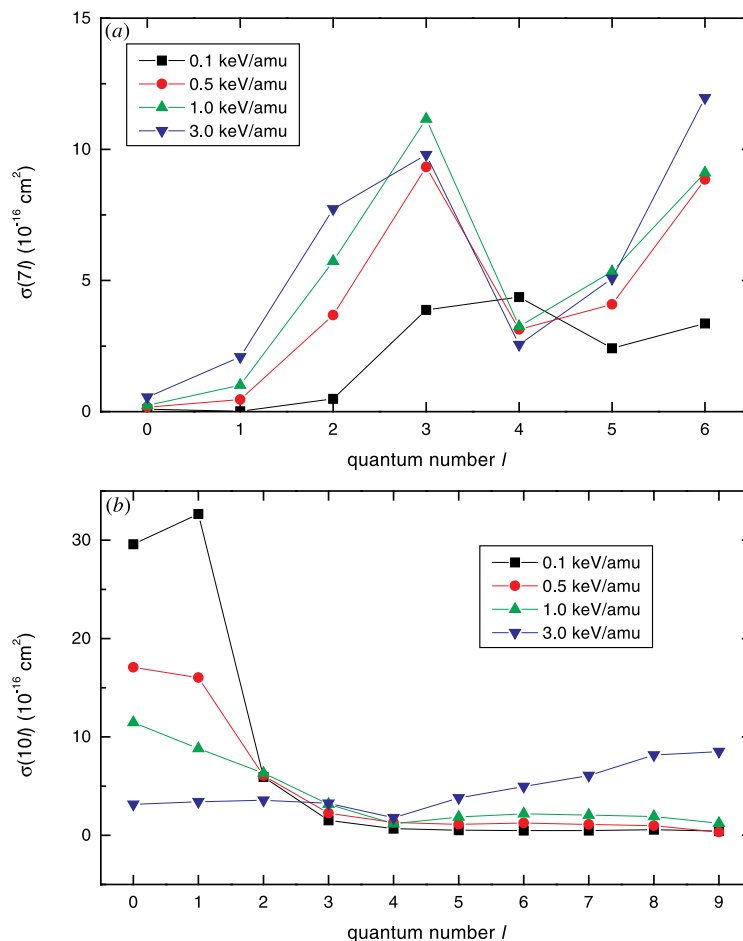


Figure 4. CTMC-calculated $n\ell$ distributions (10^{-16} cm^2) for $\text{Kr}^{8+}\text{-Li}(2s)$ collisions. The curves have been drawn to help guide the eye. (a) $n = 7$; (b) $n = 10$.

the $\sigma(8p)$ and $\sigma(7f)$ cross sections at $E \approx 1\text{--}2 \text{ keV amu}^{-1}$. Moreover, the $\sigma(8d)$ cross section goes through a well defined maximum at $E \approx 0.8 \text{ keV amu}^{-1}$, as does the $\sigma(9s)$ cross section at $E \approx 0.5 \text{ keV amu}^{-1}$. Above these electron capture channels, all the $\sigma(n\ell)$ cross sections for the non-degenerate $9p$, $8f$, $9d$, $10s$, $10p$ and $9f$ levels decrease more or less quickly with increasing energy. This demonstrates the importance of primary radial couplings for populating the non-degenerate $n\ell$ levels, which depends on the energy splittings at the avoided crossings between the entrance channel and the electron capture molecular channel (see figure 2).

It is also observed (figures 5 and 6) that even the $\sigma(8g)$ and the $\sigma(9g)$ cross sections decrease more or less quickly with increasing energies. This may be attributed to radial couplings at the avoided crossings between these electron capture channels and those associated with the $8f$ and $9f$ levels (figure 2).

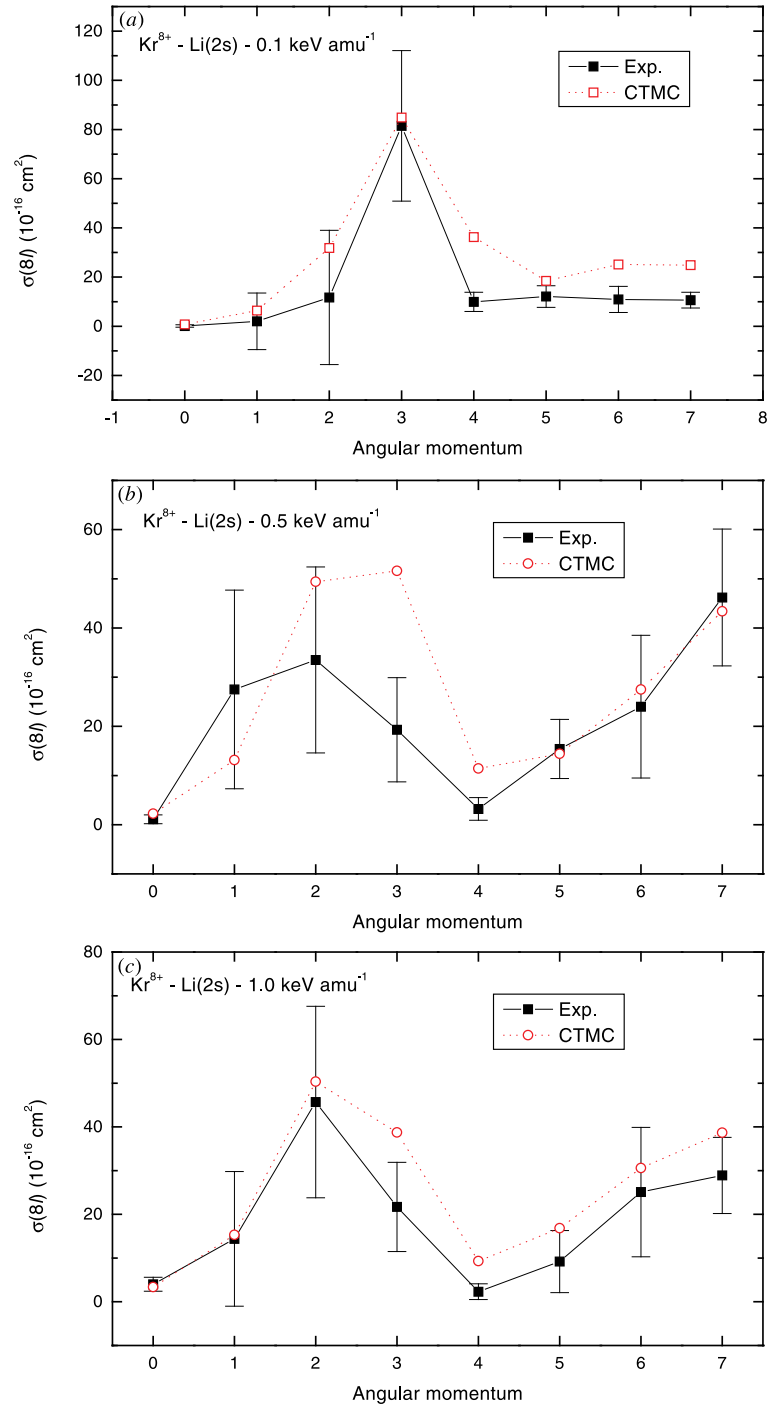


Figure 5. Experimental and CTMC-calculated 8ℓ distributions (10^{-16} cm^2) for $\text{Kr}^{8+} - \text{Li}(2s)$ collisions. The curves have been drawn to help guide the eye. (a) 0.1 keV amu^{-1} ; (b) 0.5 keV amu^{-1} ; (c) 1.0 keV amu^{-1} .

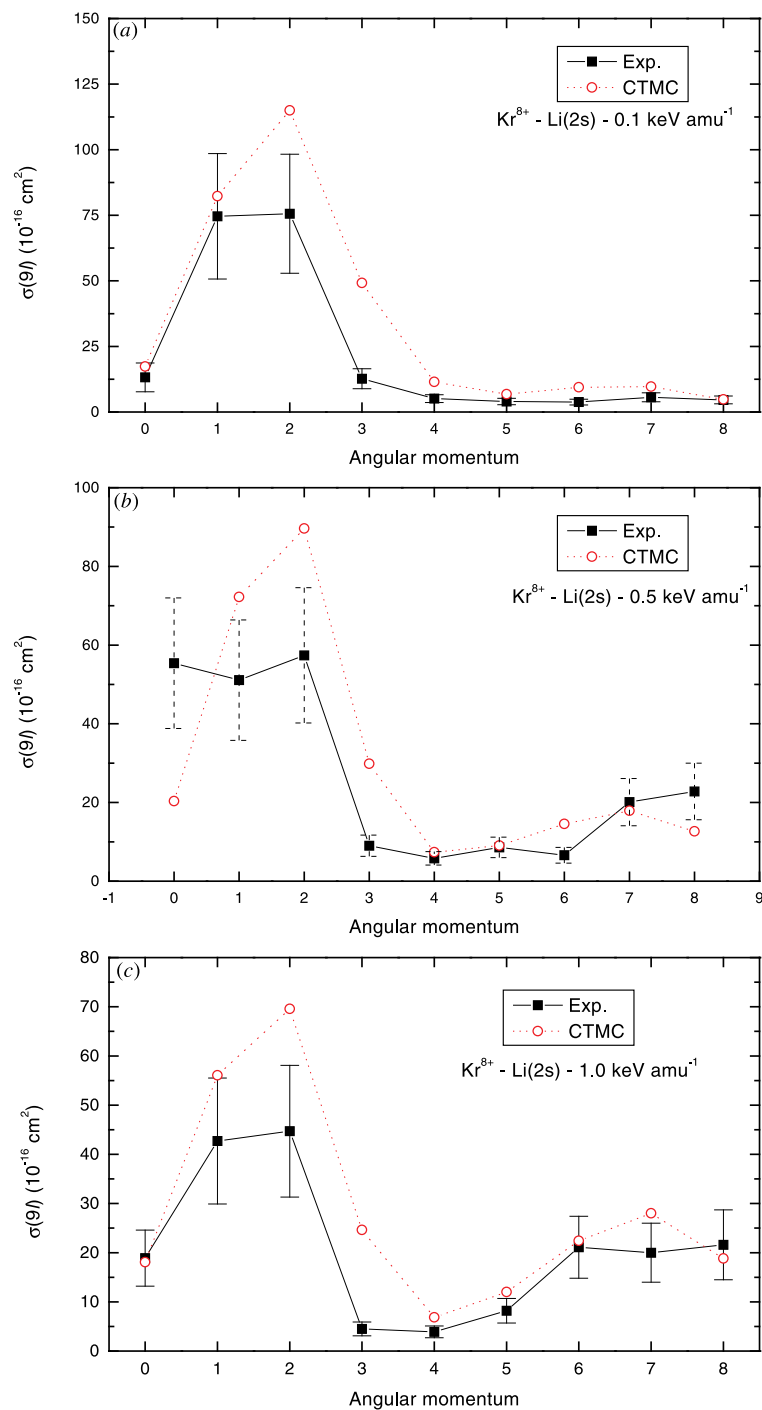


Figure 6. Experimental and CTMC-calculated 9ℓ distributions (10^{-16} cm^2) for $\text{Kr}^{8+}\text{-Li}(2s)$ collisions. The curves have been drawn to help guide the eye. (a) 0.1 keV amu^{-1} ; (b) 0.5 keV amu^{-1} ; (c) 1.0 keV amu^{-1} .

For electron capture into the degenerate $n\ell$ levels (large values of ℓ), the $\sigma(n\ell)$ cross sections increase more or less quickly with increasing energies. This indicates that these degenerate levels are populated at large internuclear distances by the Stark effect due to the residual Li^+ ion from the nf and ng electron capture molecular channels, and probably also for the $(n+1)p$ molecular channels by rotational coupling, these non-degenerate levels being themselves primarily populated by radial couplings.

5. Conclusion

In summary, we have made an extensive study of $\text{Kr}^{8+}\text{-Li}(2s)$ collisions for low projectile energies. The experimental study has been made for collision energies between 0.1 and 1.5 keV amu^{-1} by means of near-UV and visible high-resolution photon spectroscopy. Emission cross sections of each transition resulting from single electronic capture were determined using the spectroscopic response of the optical device and absolute calibration of line intensities. For the most populated $n = 8$ and 9 levels, the absolute experimental $\sigma(n\ell)$ cross sections were determined from emission cross sections and transition probabilities. Cross sections for capture into the different $n\ell$ levels were calculated using the CTMC method for collision energies from 0.1 to 5.0 keV amu^{-1} in order to make comparisons between the $\text{Kr}^{8+}\text{-Li}$ collision system and the O^{8+} and $\text{Ar}^{8+}\text{-Li}(2s)$ collision systems studied previously. Experimental and CTMC-calculated cross sections are in fair agreement on the whole, but some discrepancies are quite significant which can be attributed to experimental difficulties in discriminating between degenerate levels. Electronic energies of the one-electron $\{\text{Kr}^{7+} + \text{Li}\}^+$ system have been determined from linear combination of atomic orbitals calculations using a pseudopotential method. The analysis of the molecular electronic energy curves in connection with the CTMC results of the $\sigma(n\ell)$ cross sections has showed the first importance of primary radial couplings for populating the non-degenerate $n\ell$ levels (low ℓ values) and the importance of the Stark effect due to the residual Li^+ ion for populating degenerate $n\ell$ levels (high ℓ values) from nf and ng states and probably also from $(n+1)p$ levels by rotational coupling. This qualitative discussion based on molecular considerations seems to explain, on the whole, the energy dependence of the CTMC-calculated final n and $n\ell$ distributions for the O^{8+} , Ar^{8+} and $\text{Kr}^{8+}\text{-Li}(2s)$ collisions in the 0.1–5.0 keV amu^{-1} energy range. It is worthwhile noting that this molecular analysis of our results is also supported by the examination of some calculated classical trajectories. At the lowest energies, the valence electron is seen to move from one ionic core to the other one before being captured by the projectile, indicating clear evidence of a molecular complex formation during the collision. Comparisons of the classical results with quantal or semiclassical results would perhaps support more convincingly our CTMC calculations in the quasi-molecular domain. As already pointed out elsewhere (see Laulhé *et al* 1997), in view of the large number of electron capture channels which are involved in the present collisions, it is illusory however trying to calculate all radial and rotational couplings for solving close-coupling equations to determine state-selective electron capture cross sections. In the case where only a few reaction channels are involved in the collisions, recent quantal and semiclassical calculations have shown a qualitative agreement with CTMC calculations (Schultz *et al* 1997, Hansen *et al* 1998), indicating an apparent ability of the CTMC method to reflect some quantal features in the low-energy range. However, more theoretical work is undoubtedly needed to clearly demonstrate how the classical calculations may simulate quantal effects as there are dynamical couplings between molecular states.

Analysis of measurements of polarization rates for the emission lines following electron capture by the projectile are in progress and will be compared with the theoretical ones determined from the CTMC-calculated $\sigma(n\ell m_\ell)$ cross sections.

Acknowledgments

The experiments could not be performed without the efficient support of the staff of the GANIL test bench and the technicians of the LSA laboratory. It is a pleasure to acknowledge all of them.

References

- Abrines R and Percival I C 1966 *Proc. Phys. Soc.* **88** 861
- Aumayr F, Schorn R P, Pöckl M, Schweinzer J, Wolfrum E, McCormick K, Hintz E and Winter H P 1992 *J. Nucl. Mater.* **196-8** 928
- Brazuk A, Winter H, Dijkkamp D, de Heer F J and Drentje A G 1985 *Nucl. Instrum. Methods B* **9** 442
- Denis A, Martin S, Chen L and Désesquelles J 1994 *Phys. Rev. A* **50** 2263
- Desclaux J-P 1973 *At. Data Nucl. Data Tables* **12** 311
- Dijkkamp D, Brazuk A, Drentje A G, de Heer F J and Winter H P 1984 *J. Phys. B: At. Mol. Phys.* **17** 4371
- Gauntt D M and Danzmann K 1992 *Phys. Rev. A* **46** 5580
- Hansen J P, Kocbach L, Synnes S A, Wang J B and Dubois A 1998 *Phys. Rev. A* **57** R4086
- Hoekstra R 1995 *Comment. At. Mol. Phys.* **30** 361
- Hoekstra R, Olson R E, Folkerts H O, Wolfrum E, Pascale J, de Heer F J, Morgenstern R and Winter H P 1993 *J. Phys. B: At. Mol. Opt. Phys.* **26** 2029
- Hoekstra R, Wolfrum E, Beijers J P M, de Heer F J, Winter H P and Morgenstern R 1992 *J. Phys. B: At. Mol. Opt. Phys.* **25** 2587
- Jacquet E, Boduch P, Chantepie M, Laulhé C, Lecler D, Pascale J and Wilson M 1998 *Phys. Scr.* **58** 570
- Jacquet E, Pascale J, Boduch P, Chantepie M and Lecler D 1995 *J. Phys. B: At. Mol. Opt. Phys.* **28** 2221
- Jacquet E *et al* 1993 *Phys. Scr.* **47** 618
- 1994 *Phys. Scr.* **49** 154
- Johnson W R, Kolb D and Huang K N 1983 *At. Data Nucl. Data Tables* **28** 33
- Klapish M 1971 *Comput. Phys. Commun.* **2** 239
- Laulhé C, Jacquet E, Boduch P, Chantepie M, Ghérardi N, Husson X, Lecler D and Pascale J 1997 *J. Phys. B: At. Mol. Opt. Phys.* **30** 2899
- Martin S, Denis A, Ouerdane Y, Carré M, Buchet-Poulizac M C and Désesquelles J 1992 *Phys. Rev. A* **46** 1316
- McCormick K and the ASDEX team 1985 *Rev. Sci. Instrum.* **56** 1063
- Olson R E, Pascale J and Hoekstra R 1992 *J. Phys. B: At. Mol. Opt. Phys.* **25** 4241
- Olson R E and Salop A 1977 *Phys. Rev. A* **16** 531
- Pascale J, Olson R E and Reinhold C O 1990 *Phys. Rev. A* **42** 5305
- Pascale J, Laulhé C, Jacquet E, Boduch P and Chantepie M 1997 *Proc. 20th Int. Conf. on the Physics of Electronic and Atomic Collisions* ed F Aumayr, G Betz and H P Winter Abstract TH145
- Reader J, Acquista N and Kaufman V 1991 *J. Opt. Soc. Am. B* **8** 538
- Reinhold C O and Falcon C A 1986 *Phys. Rev. A* **33** 3859
- Rieger G, Boduch P, Chantepie M, Jacquet E, Lecler D and Pascale J 1995 *J. Phys. B: At. Mol. Opt. Phys.* **28** 2689
- Schorn R P, Hintz E, Rüsbuldt D, Aumayr F, Schneider M, Unterreiter A and Winter H P 1991 *Appl. Phys. B* **52** 71
- Schorn R P, Wolfrum E, Aumayr F, Hintz E, Rüsbuldt D and Winter H P 1992 *Nucl. Fusion* **32** 351
- Schultz D R, Reinhold C O and Krstic P S 1997 *Phys. Rev. Lett.* **78** 2720
- Schweinzer J, Wolfrum E, Aumayr F, Pöckl M, Winter H P, Schorn R P, Hintz E and Unterreiter A 1992 *Plasma Phys. Control. Fusion* **34** 1173
- Schweinzer J, Wutte D and Winter H P 1994 *J. Phys. B: At. Mol. Opt. Phys.* **27** 137
- Theodosiou C E, Inokuti M and Manson S T 1986 *At. Data Nucl. Data Tables* **35** 473
- Wolfrum E, Hoekstra R, de Heer F J, Morgenstern R and Winter H P 1992 *J. Phys. B: At. Mol. Opt. Phys.* **25** 2697
- Wutte D, Janev R K, Aumayr F, Schneider M, Schweinzer J, Smith J J and Winter H P 1997 *At. Data Nucl. Data Tables* **65** 155